Divertor detachment in the pre-fusion power operation phase in ITER during application of resonant magnetic perturbations

H Frerichs[1], X Bonnin[2], Y Feng[3], L Li[4], Y Q Liu[5], A Loarte[2], R A Pitts[2], D Reiter[6], O Schmitz[1]

[1] Department of Engineering Physics, University of Wisconsin - Madison, Madison, WI 53706, USA

[2] ITER Organization, Route de Vinon-sur-Verdon, CS 90 046, 13067 St Paul Lez Durance Cedex, France

[3] Max-Planck-Institut für Plasmaphysik, 17491 Greifswald, Germany

[4] College of Science, Donghua University, Shanghai 201620, People's Republic of China

[5] General Atomics, PO Box 85608, San Diego, CA 92186-5608, USA

[6] Institute for Laser and Plasma Physics, Heinrich-Heine-University, 40225 Düsseldorf, Germany

E-mail: `hfrerichs@wisc.edu`

Abstract. Detachment of the divertor plasma during application of resonant magnetic perturbation (RMP) fields is evaluated for hydrogen H-mode plasma during the first pre-fusion power operation (PFPO-1) phase in ITER by 3-D plasma boundary modeling with EMC3-EIRENE. Plasma response effects from a linearized, resistive, single fluid MHD model are discussed, which includes partial screening of the externally applied field - but also field amplification near the separatrix. This field amplification is found to play a pivotal role for the magnetic footprint on the divertor targets, but is sensitive to model parameters. Extensions of the footprint beyond the straight portions of the ITER vertical divertor targets, optimized for high stationary heat flux handling, may be possible depending on the level of toroidal rotation in the plasma. Exhaust from the bulk plasma is guided by the helical corrugations (lobes) of the perturbed separatrix, and this results in an upstream heat flux that is distributed over these lobes with lower peak values than in the typical radial heat flux profiles seen in the absence of magnetic perturbations. As a consequence, an earlier onset (with respect to the upstream density) of detachment is found in the traditional strike zone when RMPs are applied, but secondary, non-axisymmetric strike locations appear - and those remain attached at temperatures above $10\,\mathrm{eV}$. Neon seeding can mitigate these non-axisymmetric heat loads, but this becomes less efficient for large magnetic footprints.

(Some figures in this article are in colour only in the electronic version)

1. Introduction

The ITER project aims at a burning plasma as the next step towards fusion energy production [1]. This, however, implies that a significant amount of power needs to be exhausted from the core plasma, and this occurs through a very thin scrape-off layer (SOL) just outside the magnetic separatrix. Fast transport along magnetic field lines results in small exposed areas on the divertor targets, and even though the tungsten ITER divertor is designed to handle stationary heat fluxes of $10\,\mathrm{MW\,m^{-2}}$ [2, 3] (after toroidally averaging over the monoblock surface shaping), dissipation of a large fraction of this power is required before it can be deposited on material surfaces. Therefore, it is anticipated to operate the ITER divertor in a partially detached state [4, 5, 6] which is sufficiently deep to reduce peak heat loads, yet stable enough to maintain control over the amount and location of the dissipated power. Extensive plasma boundary modelling with the SOLPS-4.3 and SOLPS-ITER codes has been conducted to guide the design of the ITER divertor [3, 7, 8] for operation in such a partially detached state. Characterization of divertor heat loads and demonstration of their control is an integral part of the "staged approach" towards burning plasma operation outlined in the ITER Research Plan [1] with two pre-fusion power operation (PFPO) phases at lower power and magnetic field.

Another major challenge is related to the control of transient heat loads from edge localized modes (ELMs) [9], an MHD instability occurring in the edge of standard high confinement (H-mode) plasmas, since peak ELM-induced power densities can exceed the stationary loads by orders of magnitude and cause localized melting of the tungsten divertor monoblocks. Suppression or mitigation of ELMs has been successfully demonstrated in many present day tokamak experiments by application of resonant magnetic perturbations (RMPs) [10, 11, 12, 13], which are now an integral part of the ELM control scheme for ITER [14]. The perturbation field $\mathbf{B}_{\mathrm{RMP}}$ will be applied in ITER through 3 rows of 9 in-vessel window frame coils (see figure 1). These can be powered individually to produce a number of different toroidal base modes n, and fine tuning of the perturbation field is possible by varying the phase of the perturbation between rows.

Despite the small amplitude of the symmetry-breaking $\mathbf{B}_{\mathrm{RMP}}$ relative to the axisymmetric equilibrium field $\mathbf{B}_{\mathrm{equi}}$ (about 10^{-4} on the high field side to 10^{-2} on the low field side just inside the separatrix), the impact of RMP fields on the boundary plasma can be quite significant. Magnetic island chains appear where $\mathbf{B}_{\mathrm{RMP}}$ is resonant with the helical pitch $q = m/n$ (safety factor) of $\mathbf{B}_{\mathrm{equi}}$, and neighboring island chains can overlap to form a layer with chaotic or so-called "stochastic" field line trajectories. This island overlap is most relevant at the plasma edge in poloidally diverted plasmas where resonances are located closer and closer together towards the magnetic separatrix. The perturbed magnetic separatrix develops helical corrugations (referred to as lobes) which become more dense and elongated towards the X-point, which is a well known phenomenon in nonlinear dynamics in perturbed systems with
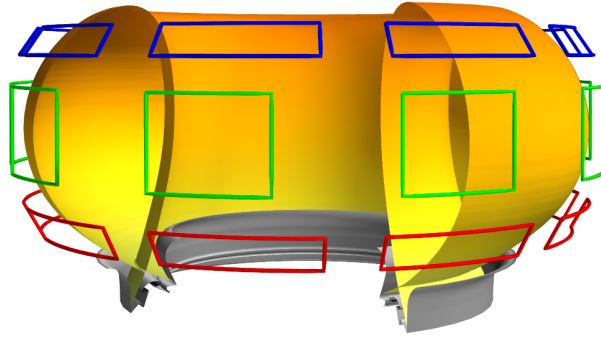
Figure 1. In-vessel coils for application of resonant magnetic perturbations in ITER. A scrape-off layer equilibrium flux surface and the divertor targets are shown for reference.

a hyperbolic fixed point [15, 16]. Magnetic field lines can thereby escape from the chaotic layer in the bulk plasma‡ and are guided by the perturbed separatrix towards a non-axisymmetric strike zone on the divertor targets [17]. This acts as a new exhaust channel that can largely replace the traditional SOL (outside the magnetic separatrix), and corresponding striation patterns in particle and heat loads have been observed in contemporary experiments (ASDEX Upgrade [18], DIII-D [19, 20], EAST [21], JET [22], KSTAR [23], NSTX [24]).

These effects, however, have not been taken into account during the design of the ITER divertor since the SOLPS suite of codes exploits the traditional approximation of toroidal symmetry in tokamak configurations so that model equations can be simplified to two dimensions for efficiency. Nevertheless, symmetry-breaking effects from RMP application can be taken into account by moving from SOLPS to the 3-D computational model EMC3-EIRENE [25, 26]. This is less complete in terms of physics contained in the SOLPS fluid plasma solver (B2.5) - for example, drifts and currents are not yet included in the EMC3 code - but the kinetic neutral solver (EIRENE) is used in both. Even though EMC3-EIRENE has been originally developed for stellarators, it has already been extended for efficient application to poloidal divertor tokamak configurations with RMPs [27]. Previously, an initial exploration of RMP effects in ITER has been conducted [28], but only for attached divertor conditions because at the time EMC3-EIRENE (when applied to ITER) was unable to properly access the detached state due to numerical oscillations and missing volumetric recombination. Despite some initial success in stabilizing the iterative procedure of EMC3-EIRENE through adaptive relaxation [29], numerical access to a detached divertor state has remained challenging for EMC3-EIRENE. Only recently has more robust stabilization been achieved based on a linearization of the electron energy loss term from interaction with neutral gas [30]. Furthermore, volumetric recombination has been implemented into EMC3-EIRENE now

‡ In the following we will use the phrase *bulk plasma* instead of *confined plasma* for the plasma domain inside the magnetic separatrix of the unperturbed equilibrium configuration, thereby acknowledging the fact that some field lines may no longer be confined to this region once RMPs are applied.

[31] and evaluated for ASDEX Upgrade [32].

With this upgrade of EMC3-EIRENE, we can now analyze the impact of RMPs on divertor detachment in ITER for the first time, and we begin with an evaluation for the first PFPO phase here (PFPO-1). During this phase, ITER hydrogen H-mode plasmas will be first explored (among other targets) at reduced field (1.8 T) and plasma current (5 MA) since for these conditions ELM energy loads are not expected to cause tungsten monoblock melting [33]. These plasmas will operate at typical power levels of $(20 - 30\,\mathrm{MW})$ by the use of ECH (3rd harmonic) on its own (assuming that a presently considered upgrade of the ECH power by 10 MW is implemented by the beginning of PFPO), or in combination with ICH (majority heating) or NBI at reduced beam injection energy later in PFPO-2 [34, 35]. These plasmas will have the same $q_{95} \approx 3$ as anticipated for the fusion power operation (FPO) phase with a burning plasma $(Q = 10)$. This is an ideal test bed for RMP application, because resonances will be at similar radial positions throughout the plasma (resulting in a similar magnetic field geometry in the plasma boundary), while power handling requirements are much less restrictive as for the FPO phase. It will therefore be possible to explore the transition from attached to detached states, whilst during high power operation in FPO, the attached divertor state will be completely inaccessible from the point of view of divertor target power handling. Our focus is on application of RMPs with $n = 3$ toroidal symmetry with a phasing that has been optimized for ELM control (by maximizing the plasma displacement near the X-point which is often associated with the edge-peeling response) [36, 37] based on MARS-F [38, 39]. We will begin with a brief description of the EMC3-EIRENE model for the plasma boundary in Section 2, and continue with a discussion of plasma response effects. In particular, in Section 2.1, we evaluate plasma response with respect to the magnetic geometry from the externally applied field (vacuum RMP approximation), and in Section 2.2 we address how model assumptions for the plasma response affect simulation results. Then, in Section 3, we investigate the impact of RMPs on detachment with focus on the particle flux roll-over in Section 3.1, and include dissipation from Neon seeding in Section 3.2. Finally, open questions are discussed in Section 4.

2. Plasma boundary modelling with RMPs

The boundary plasma in EMC3-EIRENE (as well as SOLPS-ITER) is based on a fluid model in which local values for density n_i, Mach number M (flow velocity $u_\parallel$ normalized to sound speed c_s) and temperatures T_e, T_i are determined by steady state balance equations (for an extensive description of the model equations see e.g. references [25, 31]):

$$\nabla \cdot \mathbf{\Gamma} = S_p \tag{1}$$

$$\nabla \cdot \left(m_i\, u_\parallel\, \mathbf{\Gamma} - \boldsymbol{\tau} \right) = -\nabla_\parallel p + S_m \tag{2}$$
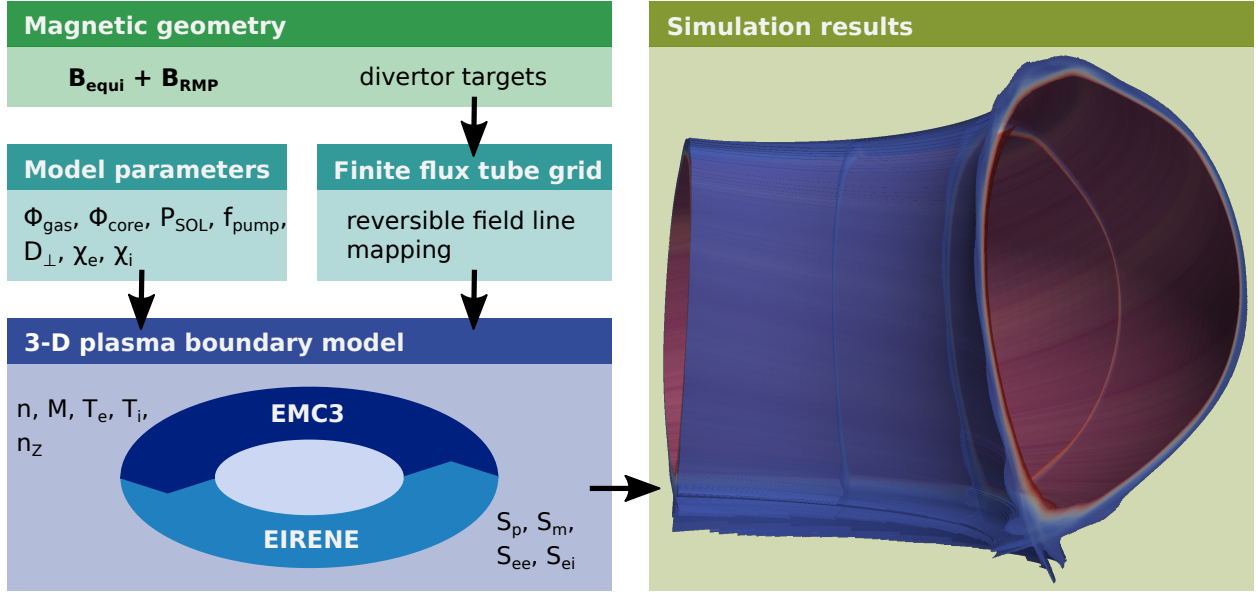
Figure 2. The EMC3-EIRENE model for a 3-D plasma boundary: the magnetic geometry (and divertor targets) is required input along with model parameters for particle and power throughput, and anomalous cross-field transport. The resulting 3-D T_e from RMP application is shown on the right.

$$\nabla \cdot \mathbf{q}_e = S_{ee} \qquad \nabla \cdot \mathbf{q}_i = S_{ei} \qquad (3)$$

The compact form (1) denotes the balance between changes in particle flux $\mathbf{\Gamma}$ and particle sources S_p from ionization of neutrals or sinks from recombination. Quasi-neutrality $n_e \approx n_i$ is assumed, and $\mathbf{\Gamma}$ includes anomalous cross-field transport through a model parameter $D_\perp = 0.3\,\mathrm{m^2\,s^{-1}}$. Momentum along field lines is driven by the pressure gradient, and can be transferred between ions and neutral particles through charge-exchange. Viscosity $\boldsymbol{\tau}$ is classical along the field line direction and implicitly set to $\eta_\perp = m_i\,n_i\,D_\perp$ in the cross-field directions. The energy balance equations for electrons and ions include conduction and convection on the left hand side, and are coupled through an exchange term on the right hand side. Conduction along field lines is classical while a model parameter $\chi_\perp = 1\,\mathrm{m^2\,s^{-1}}$ accounts for anomalous cross-field heat transport. Both $D_\perp$ and $\chi_\perp$ are set to the standard values used for the majority of SOLPS-ITER simulations [3]. Furthermore, energy losses from radiation, molecular dissociation, and ionization are included on the right hand sides of (3). This may include energy losses from impurities in a *trace* approximation (which is defined here as negligible contribution to n_e, and thermal equilibrium with the main ion species $T_Z \approx T_i$). Ionization and recombination is included in the impurity particle balance for charge stage Z, and transport is determined by a balance between friction and thermal forces.

Following the approach of SOLPS-ITER and other 2-D plasma boundary models, equations (1)-(3) are solved for a fixed magnetic geometry. Unlike 2-D models, however, EMC3-EIRENE needs to account for the symmetry-breaking perturbation field $\mathbf{B}_{\mathrm{RMP}}$.

A representation of the magnetic geometry in the form of a finite flux tube grid is constructed first (as indicated in figure 2), and field lines are reconstructed from this grid in EMC3-EIRENE based on a reversible field line mapping technique [40]. While this is done for numerical efficiency, it also detaches EMC3-EIRENE itself from the model that provides $\mathbf{B}_\mathrm{RMP}$ (and $\mathbf{B}_\mathrm{equi}$). Historically, the so-called *vacuum approximation* of the external perturbation field $\mathbf{B}_\mathrm{vacuum\ RMP}$ is applied based on a polygonal representation of the coils and the Biot-Savart law. However, the magnetic geometry can be modified by an internal response $\mathbf{B}_\mathrm{response}$ of the plasma. This plasma response can be taken into account, but it has to be provided by an external model for a total $\mathbf{B}_\mathrm{RMP} = \mathbf{B}_\mathrm{vacuum\ RMP} + \mathbf{B}_\mathrm{response}$ that can be used for tracing field line segments to construct the finite flux tube grid. In the following we exploit recent MARS-F results [36, 37] based on a single fluid, linearized, resistive magneto-hydrodynamics (MHD) model for $\mathbf{B}_\mathrm{RMP}$ (see e.g. reference [41] for a brief review of present MHD models for plasma response). At this point, no feedback from the plasma boundary simulation on the plasma response is taken into account. As an intermediate step, however, the impact of model assumptions that go into the plasma response will be addressed in Section 2.2.

A self-consistent solution for the plasma boundary is obtained by iterating between EMC3 and EIRENE for the left and right hand sides of (1)-(3), respectively. Model equations are constrained by the total particle throughput (gas puff Φ_gas as scan parameter and fixed core fueling $\Phi_\mathrm{core} = 5 \cdot 10^{20}\,\mathrm{s}^{-1}$ from neutral beam and/or pellet injection which is balanced by pumping), and power input is set to $P_\mathrm{SOL} = 30\,\mathrm{MW}$ as representative for PFPO-1 for H-modes at 1.8 T with 5 MA of plasma current. Recycling on the divertor surfaces (release of neutral particles after recombination of the incoming ions and electrons) is set to 100 %, which implies that the density at the core boundary is a dependent parameter determined by the particle throughput. Pumping of neutral gas from below the dome is accounted for with a sticking factor of $f_\mathrm{pump} = 0.72\,\%$, and the dome support structure (dashed lines in figure 4) is approximated by semi-transparent surfaces with a reflection probability of 50 %, consistent with SOLPS-ITER modeling (see e.g. figure 3 in reference [3]). Radiation from impurities is not included here (because impurity seeding is not anticipated for PFPO-1), but will be briefly explored later in Section 3.2.

2.1. Comparison to vacuum RMP approximation

The externally applied perturbation field (without plasma response) leads to the formation of a set of fairly large island chains at positions where the helical pitch $q = m/n$ (safety factor) has a rational value. A layer with chaotic (often referred to as stochastic) field line trajectories results when adjacent island chains begin to overlap. This magnetic geometry is shown by the Poincaré plot in figure 3 (a), where the position of the resonances for the $n = 3$ RMP field has been marked by horizontal lines. The last closed magnetic flux surface is located at a normalized poloidal flux of $\psi_N = 0.65$ which is located below the $m = 6$ resonance). However, an approximate flux surface can be
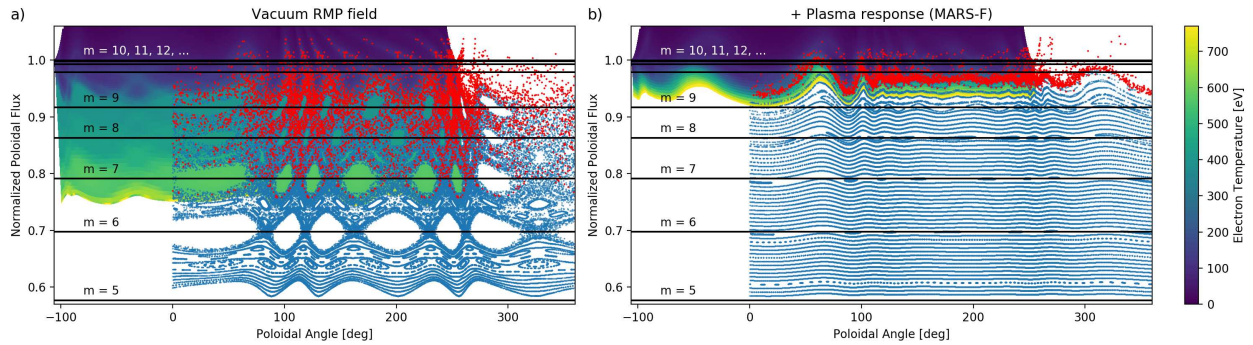
Figure 3. Simulation results for T_e (colour shaded regions) based on (a) the vacuum RMP approximation and (b) with plasma response included for the same particle throughput of $\Phi_{\mathrm{gas}} = 3 \cdot 10^{22}\,\mathrm{s}^{-1}$. Poincaré plots show the magnetic geometry with red points corresponding to field lines that connect to the divertor targets. The radial position of the resonances $q = m/n$ for the $n = 3$ RMP field is indicated by black lines.

found between the $m = 6$ and $m = 7$ resonances at $\psi_N = 0.77$, and this is taken as the inner boundary for the EMC3-EIRENE simulation. Within the first 100 field periods, field lines have a standard devition of $\delta\psi_N = 3.6 \cdot 10^{-3}$ from this approximate surface. It can be seen that remnant island chains are present throughout the edge, but also that the chaotic regions are connected with field lines escaping to the divertor targets (red). Nevertheless, only a few field lines connect from $\psi_N < 0.82$, and this indicates the presence of a *ghost surface* which is known to coincide with isotherms [42]. Indeed, the resulting T_e in figure 3 (a) from EMC3-EIRENE remains rather flat at either side of $\psi_N \approx 0.82$ at values of about $560\,\mathrm{eV}$ and $420\,\mathrm{eV}$, respectively.

The Poincaré plot in figure 3 (b) shows the magnetic geometry with plasma response included. The ideal MHD plasma is expected to shield the resonances of the external perturbations, but reconnection of field lines and formation of island chains is possible with finite resistivity. It can be seen that resonances are still mostly screened throughout the plasma, but a small chaotic layer with escaping field lines (red) exists outside $\psi_N \approx 0.94$. Higher temperatures can be sustained on good flux surfaces, and $T_e \approx 750\,\mathrm{eV}$ is found at the inner simulation boundary. This is about a factor of 2 higher than in the vacuum RMP approximation at the same radial position. Earlier EMC3-EIRENE simulations for DIII-D [43] and ITER [28] have shown a similar deficiency of the vacuum RMP approximation which is recovered once a screening plasma response is taken into account. However, unlike the *ad hoc* screening applied in those earlier simulations, the present plasma response is a result of an MHD model in full toroidal geometry. The important difference is that the MARS-F plasma response can include a field amplification near the separatrix (as we will evaluate quantitatively in Section 2.2), and it is this local field amplification that plays a pivotal role for the strike pattern of field lines connecting from the bulk plasma onto the divertor targets.

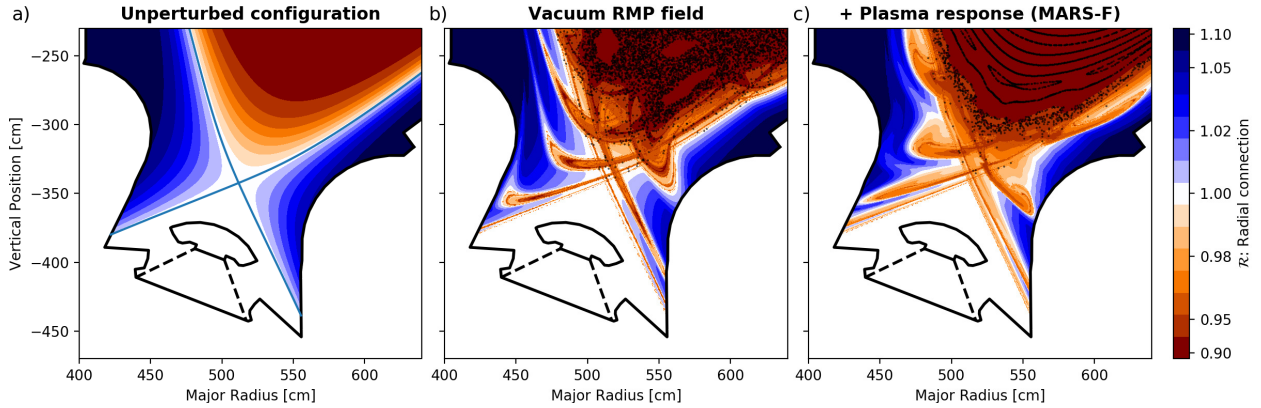A cross-section of the magnetic geometry in the divertor region is shown in figure

Figure 4. Magnetic geometry of the (a) unperturbed (reference) configuration, (b) vacuum approximation for the RMP field, and (c) plasma response scenario predicted by MARS-F. The radial connection $\mathcal{R}$ is evaluated as the minimum of ψ_N along each field line. Poincaré plots (black) show the extend of the chaotic field line domain.

4 for the vacuum RMP field and the plasma response case in comparison to the unperturbed configuration. While Poincaré plots highlight the presence of remnant island chains and chaotic layers, they provide little insight into how field lines connect between bulk plasma and divertor targets. For this we define the radial connection $\mathcal{R}$ of a field line as the minimum of ψ_N that this field line reaches along its way. An unperturbed field line never leaves its associated flux surface, and so contour lines of $\mathcal{R}$ are equivalent to the flux surface contours in the unperturbed configuration in figure 4 (a), both inside (orange) and outside (blue) the separatrix (which is added for guidance). Perturbed field lines, on the other hand, can escape the bulk plasma guided by the perturbed separatrix, and this is evident in figures 4 (b) and (c) by the orange colours which fill out the helical lobes formed by the perturbed separatrix. The darker orange colours in 4 (b) compared with (c) show a deeper radial connection, consistent with a broader chaotic layer in the vacuum RMP approximation already found in figure 3 (a). What is notable here, however, is that the size of these helical lobes is similar in 4 (b) and (c) despite the screening nature of the plasma response.

Below we will evaluate the resulting impact on the (outer) divertor target, and for this we first discuss the unperturbed configuration as reference case: the toroidally symmetric magnetic footprint on the outer divertor target is shown in figure 5 (a), and the resulting heat load is given in figure 5 (d). The primary SOL (with $\mathcal{R}$ shown in white) connects a layer of a few mm radial width from the outboard midplane to the target, and this is where the power exhaust originates from upstream (as we shall quantify in section 3.1). Downstream (within the divertor), heat flux is then spread out into the private flux region (PFR) and into the near SOL. The latter is shown in light blue in figure 5 (a), and the resulting heat loads are evident in 5 (d). In the following, we will refer to the first $\sim 8\,\mathrm{cm}$ from the reference separatrix strike point as the *traditional strike zone*. No significant heat flux reaches the far SOL (indicated by medium to dark
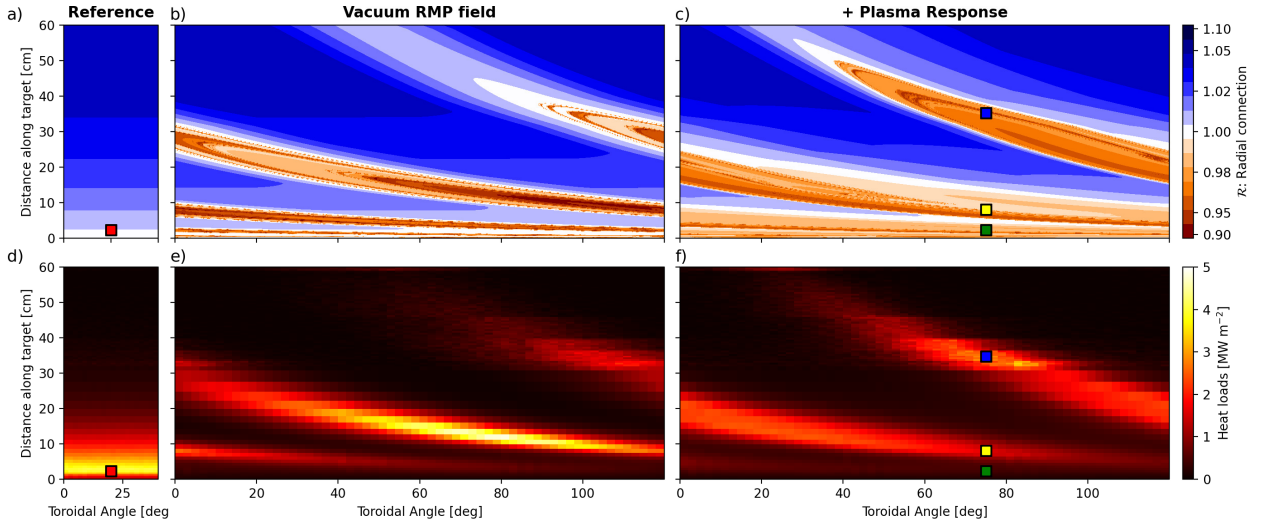
Figure 5. Upper row: magnetic footprint on the outer divertor target for configurations in figure 4, lower row: resulting heat loads obtained for the same particle throughput of $\Phi_{gas} = 3 \cdot 10^{22}\,\mathrm{s}^{-1}$ for the RMP cases (a lower throughput of $\Phi_{gas} = 1.5 \cdot 10^{22}\,\mathrm{s}^{-1}$ is selected for the reference for comparable upstream densities). Only 1/3 of the torus is shown because of the $n = 3$ symmetry of the RMP field.

blue colours) 20 cm or more away from the separatrix strike point.

This is fundamentally different once RMPs are applied: as discussed above, the perturbed separatrix guides field lines from the bulk plasma towards the targets, and this is evident by the orange colours in figures 5 (b) and (c). Let s_ψ denote the maximum distance from the reference separatrix strike point from where field lines still connect into the bulk plasma (i.e. $\mathcal{R} < 1$). The strike pattern is non-axisymmetric as a result of the helical nature of the perturbed separatrix, and the similar size of the helical lobes observed in figure 4 (b) and (c) is confirmed here. As it turns out, $s_\psi = 48.5$ cm is even a bit larger in the plasma response case (compared to $s_\psi = 38.4$ cm in the vacuum RMP approximation) despite screening of most resonances, and the corrugation of the separatrix continues as ripple into the SOL beyond s_ψ. Figures 5 (e) and (f) show that heat loads are aligned with the magnetic footprint (the same can be observed for particle loads), and in particular that most heat flux is exhausted along perturbed field lines connecting from the bulk plasma - rather than from the upstream SOL with $\mathcal{R} > 1$ (i.e. the former SOL has become a marginal extension of the new exhaust channel, although toroidal variation of the heat load is still found beyond s_ψ from the residual power exhaust that does cross the perturbed separatrix).

Although the general outline of the heat load patterns are the same with and without plasma response, substantial differences are found for the heat load peaks. Here we have selected a higher throughput of $\Phi_{gas} = 3 \cdot 10^{22}\,\mathrm{s}^{-1}$ for the RMP cases compared to $\Phi_{gas} = 1.5 \cdot 10^{22}\,\mathrm{s}^{-1}$ for the reference case, because this results in comparable *upstream densities* of $\overline{n}_{up}^{(RMP)} = (1.67 \pm 0.28) \cdot 10^{19}\,\mathrm{m}^{-3}$ (plasma response case) and $\overline{n}_{up}^{(ref.)} = (1.80 \pm 0.07) \cdot 10^{19}\,\mathrm{m}^{-3}$. Traditionally, the upstream density is evaluated at
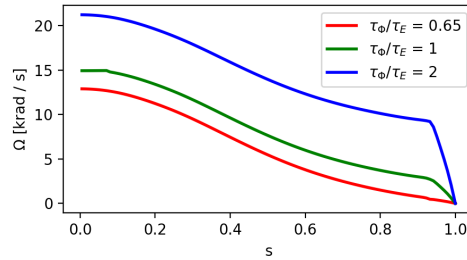
Figure 6. Flow profile inputs for MARS-F plasma response predictions for different assumptions of the ratio of toroidal momentum to thermal confinement times τ_Φ/τ_E.

the outboard midplane, but this is not a suitable approach with RMPs because of helical variations of the plasma associated with the perturbed separatrix. Therefore, we take the average along the inside of the reference separatrix (but excluding 1/8 of the poloidal circumference on either side of the X-point) as a proxy for the upstream density. This $\overline{n}_{\mathrm{up}}$ is both similar in value to the traditional approach for the unperturbed configuration, and at the same time less sensitive and more representative for the RMP cases. By comparing the heat load pattern to the radial field line connection, it can be seen that heat load peaks correspond to the deepest connection into the bulk plasma. In particular, the heat load peak of $4.8\,\mathrm{MW\,m^{-2}}$ in the vacuum RMP approximation exceeds that of $4.1\,\mathrm{MW\,m^{-2}}$ in the unperturbed reference configuration. Heat loads are more favourable in the plasma response configuration, at least with respect to the peak value of $3.4\,\mathrm{MW\,m^{-2}}$. Here, the radial connection is not as deep as in the vacuum RMP approximation, and heat loads are more evenly distributed. The location of the heat load peak, however, is significantly further away at over $30\,\mathrm{cm}$ from the reference separatrix strike point, and this can have significant impact on divertor performance as we will show below.

Common in both RMP cases with and without plasma response is that heat loads in the traditional strike zone are substantially reduced with respect to the unperturbed reference. This indicates an earlier onset of detachment, and in section 3.1 we will elaborate on this by detailed evaluation for the 3 strike points marked by the small coloured squares in figure 5 (f) compared to the one marked in (d). From now on we will put the vacuum RMP approximation aside and focus on the plasma response case. Before an analysis of RMP effects on detachment, however, we next address the importance of reliable plasma response predictions.

2.2. Sensitivity on plasma response parameters

Application of MARS-F for plasma response requires smoothing of the X-point geometry, and this can affect the edge-peeling amplification [44]. The magnetic footprint in figure 5 (c) is based on X-point smoothing which results in a safety factor of $q_a = 3.73$ at the MARS-F plasma boundary (i.e. resonances up to $m = 11$ are included). For comparison, less smoothing with $q_a = 4.07$ (which includes the $m = 12$ resonance)

results in a magnetic footprint size of $s_\psi = 42.7\,\text{cm}$ that is only $12\,\%$ smaller. However, the edge-peeling response is more pronounced with too much smoothing: at $q_a = 3.41$ (only resonances up to $m = 10$ included), the footprint size is with $s_\psi = 114.2\,\text{cm}$ more than a factor of 2 larger. Nevertheless, the lower sensitivity at higher q_a values (i.e. when approaching the true X-point geometry with less smoothing) provides reasonable confidence in the presented results.

The plasma response case discussed above is based on the assumption of *low* toroidal rotation consistent with expectations for ITER. Flow profiles for the MARS-F plasma response predictions have been computed by ASTRA transport simulations, and the key parameter considered here is the ratio of toroidal momentum to thermal confinement times τ_Φ/τ_E. Since no reliable model exist to predict intrinsic rotation in ITER, ASTRA modelling assumes that $10\,\text{MW}$ of the additional heating is provided by NBI with the associated momentum source leading to the modelled rotation profiles; otherwise the modelled rotation for RF-only heated plasmas would be zero. It should be pointed out, however, that the assumption $\tau_\Phi/\tau_E = 2$ leading to the high rotation profiles in figure 6 approximates well the results of first principle modelling [45]. The resulting flow profiles are shown in figure 6 for three different assumptions of τ_Φ/τ_E which we will refer to as low (red), moderate (green) and high rotation (blue) in the following. These cases have been analyzed with respect to ELM control in reference [37], and we extend this analysis here for its implications on the plasma boundary.

We have highlighted the impact of a screening plasma response above, and noted that local field amplification is possible as well. To distinguish between these competing effects, we resolve the poloidal harmonics of (the radial component of) $\mathbf{B}_{\text{RMP}}$. More precisely, we evaluate the Fourier spectrum of the perturbed flux $\Phi = J\,\mathbf{B}_{\text{RMP}} \cdot \nabla\psi$

$$\Phi_{mn} = \frac{1}{4\,\pi^2} \iint d\theta\, d\varphi\, e^{-i\,(m\,\theta - n\,\varphi)}\, \frac{\mathbf{B}_{\text{RMP}} \cdot \nabla\,\psi}{\mathbf{B} \cdot \nabla\theta} \tag{4}$$

which includes the Jacobian $J^{-1} = \mathbf{B} \cdot \nabla\theta$ of the straight field line coordinate system φ, θ, ψ. Furthermore, we introduce the normalized harmonics

$$\tilde{b}^1_{mn} = \frac{1}{B_0\,R_0^2}\,\Phi_{mn} \tag{5}$$

based on the toroidal field B_0 and major radius R_0 of the magnetic axis. The radial dependence of $\tilde{b}^1_{mn}$ is shown in figure 7 (a-c) for the three flow profiles from figure 6, and $\tilde{b}^1_{mn}$ from the external field is shown in the inset of figure 7 (a) for reference. Screening of the resonant field is found for all plasma response cases throughout most of the plasma, in confirmation of the narrower chaotic layer and shallower radial field line connection compared to the vacuum RMP approximation discussed in the previous section. However, screening is weaker for the moderate and high rotation plasma response case, which results in deeper field line connection compare to the low rotation case.

Here we also find confirmation for the extent of the magnetic footprint, since amplification of the non-resonant harmonics at the very edge is evident in figure 7 (a-c).
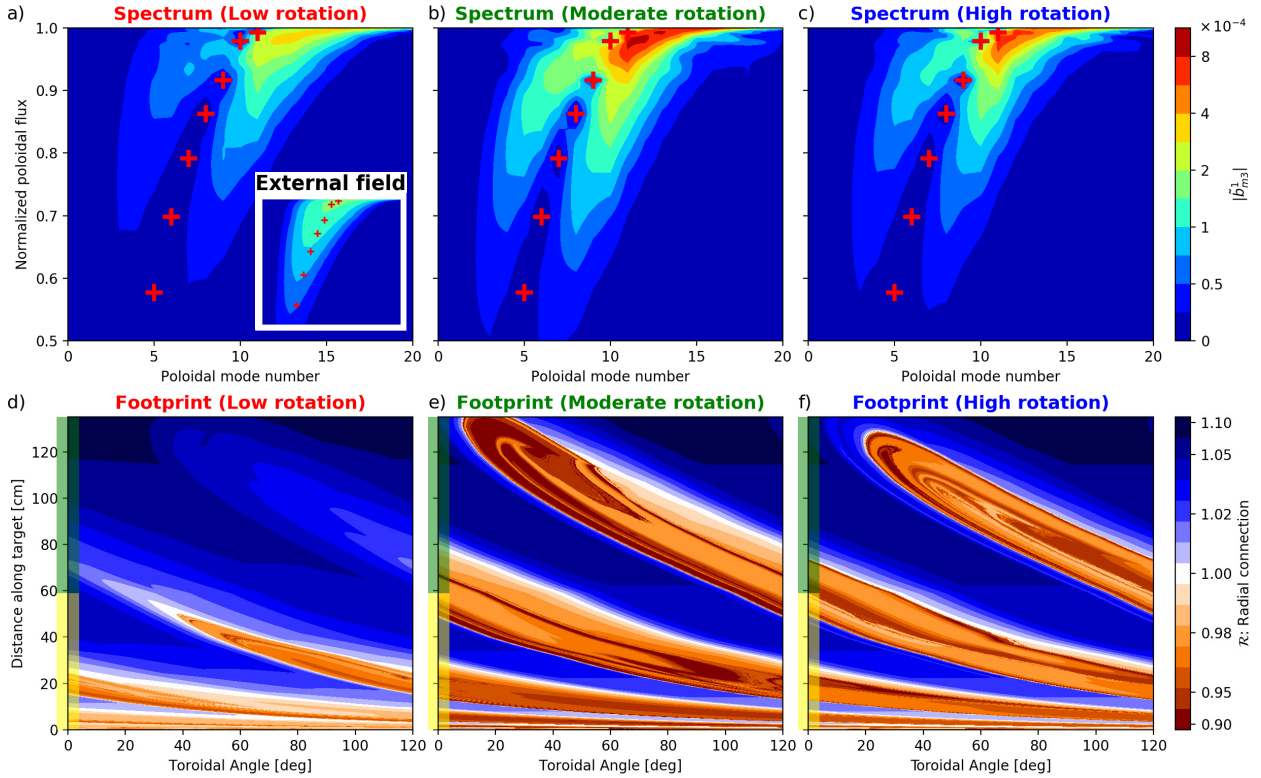
Figure 7. (a-c) Fourier spectrum of the perturbation field for the three different flow profiles from figure 6. The positions of the resonances for $n = 3$ are marked by red symbols, and the Fourier spectrum of the external field is shown as inset in (a) for reference. (d-f) The resulting magnetic footprints on the outer divertor target. The yellow bar marks the extent of the straight portion of the vertical target in which the top surfaces of the tungsten monoblocks comprising the target are toroidally bevelled to protect leading edges. The green bar marks the divertor baffle with lower stationary power handling capability.

These findings are qualitatively the same for the three different plasma response cases, but quantitative differences in the kink or edge-peeling ($m > n\,q$) response can have a huge impact on the resulting magnetic footprint size. Moderate amplification is found for the low rotation case, while strong amplification is found for the moderate and high rotation cases. Even though some variation is to be expected, it is remarkable how the rather small difference between the red and green flow profiles in figure 6 compared to the blue one results in the big difference of the edge-peeling response found in figures 7 (a) and (b). The stronger amplification is reflected in the size of the magnetic footprints, as can be seen in figures 7 (e) and (f) compared to (d). Both moderate and high rotation cases have magnetic footprints where field lines connect from the bulk plasma to the curved divertor baffle region up to 120 cm away from the reference separatrix strike point. Although it comprises the same tungsten monoblocks as in the straight portions of the ITER vertical targets, this baffle region (delimited by the green vertical bars in figure 7) will have lower stationary heat handling capability. This is because the monoblocks
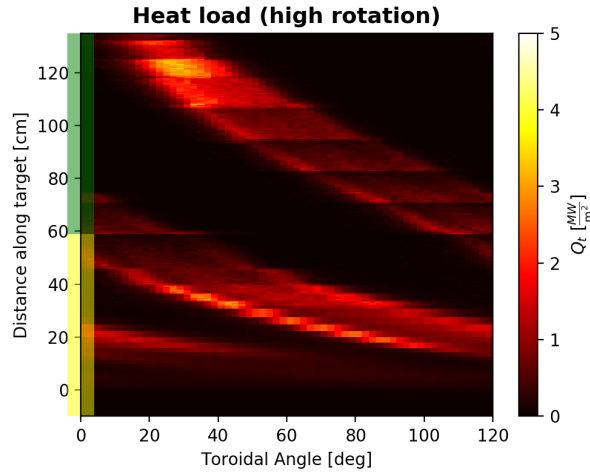
Figure 8. Heat loads for the high rotation plasma response case shown in figure 7 (f) at the same throughput of $\Phi_{\text{gas}} = 3 \cdot 10^{22} \, \text{s}^{-1}$ as the RMP cases in figure 5.

forming the straight portion of the target are toroidally bevelled on the top surface to magnetically shadow any leading edges arising as a result of radial misalignments between toroidally neighbouring units [33]. In addition, the baffle region is designed with a much deeper bevel, extending over several monoblocks on the toroidal wings of the outer vertical targets to mitigate the consequences of downward going disruption current quench plasmas [46]. As a result of the much steeper field line incidence angle, the stationary loads on these areas would limit the allowable stationary heat fluxes which could be allowed to extend up to the baffle region. Finally, the pumping efficiency for particles recycled high up on the baffle would be much lower in comparison with particle interactions concentrated deep in the vertical targets. In the following we will evaluate the resulting heat loads for such extreme magnetic footprints. We have initially chosen the high rotation case for the comparison below in order to cover the range of rotation in the set of available MARS-F data, although in retrospect it is the moderate rotation case that would make a more suitable worst case scenario because of the slightly larger magnetic footprint. Nevertheless, we expect that results are similar enough (with respect to the huge difference to the low rotation case) so that further differentiating between the moderate and high rotation case would not add any more insight.

The outer target heat loads for the high rotation plasma response case are shown in figure 8: virtually no heat loads appear within 20 cm of the reference separatrix strike point, significant heat loads $\sim 3 \, \text{MW} \, \text{m}^{-2}$ appear at the outermost part of the magnetic footprint far beyond the optimized high heat flux region (yellow). Note that already a small heat load of $\sim 0.5 \, \text{MW} \, \text{m}^{-2}$ corresponds to a parallel heat flux of $10 \, \text{MW} \, \text{m}^{-2}$ that could be deposited on any monoblocks leading edges. Therefore, heat loads beyond the optimized region should be avoided, or at least adequately mitigated. Heat loads on the curved baffle are toroidally localized to a region of about 20 deg, and so a slow (several Hz) rotation of the perturbation field may be sufficient to mitigate these loads.

Nevertheless, it is desirable to use this capability only when needed to minimize fatigue lifetime consumption of these coils. In Section 3.2 we briefly explore impurity seeding for supplemented power dissipation as a possible solution. In any case, such an extended footprint would be significantly more challenging in the burning plasma phase with 100 MW of power exhaust.

Even though the high rotation case may be less likely in the ITER PFPO phase than the low rotation case discussed in the previous section, it may still be relevant because of its similar footprint size compared with the moderate rotation case (which could be considered an upper limit of a qualitatively *low* rotation scenario). Whether the high and moderate rotation cases imply the same ELM suppression threshold as the low rotation case, however, or if a lower RMP strength is sufficient (resulting in a not quite as large a footprint), is another question that remains to be investigated. Regardless, figure 7 shows how uncertainty from an initial choice of model parameters propagates through the chain of models (ASTRA $\rightarrow$ MARS-F $\rightarrow$ EMC3-EIRENE), and may become a serious issue for predicting divertor loads. Further quantification (and verification for present experiments) is therefore advisable, but would go beyond the scope of this paper. In the following recycling analysis, we will continue to focus on the low rotation case.

3. RMP effects on detachment

We have hinted at an earlier onset of detachment in the discussion of figure 5, but this was only based on one comparison of heat loads. A characteristic feature of detachment is the roll-over of the divertor target ion (recycling) flux with increasing upstream density, and this requires evaluation of the trend through several simulations. In the following, density scans are conducted through an incremental increase of the gas puffing rate Φ_{gas}, and the role of power and pressure losses in the divertor volume is evaluated in section 3.1. Then, supplemental dissipation from Neon seeding is briefly explored in section 3.2.

3.1. Recycling characteristics

The density dependence of the recycling flux is evaluated at the 3 example strike points with field line connection from the bulk plasma for the plasma response RMP case from figure 5, and shown in figure 9: SP 1 (green) in the traditional strike zone at $s_1 = 2.3\,\mathrm{cm}$ from the reference separatrix strike point (connecting from within 4 mm distance at the outboard midplane), SP 2 (yellow) at the edge of the traditional strike zone at $s_2 = 7.0\,\mathrm{cm}$, and SP 3 (blue) in the reference far SOL at $s_3 = 34.7\,\mathrm{cm}$. It can be seen that $\overline{n}_{\mathrm{up}}$ at recycling flux roll-over for SP 1 is significantly lower than for the reference case without RMPs (red) evaluated at the same location, and that the detachment transition has already occurred at SP 1 in the simulation shown in figure 5 (f) but not in (d) without RMPs. SP 2 is just at the roll-over point, while SP 3 remains
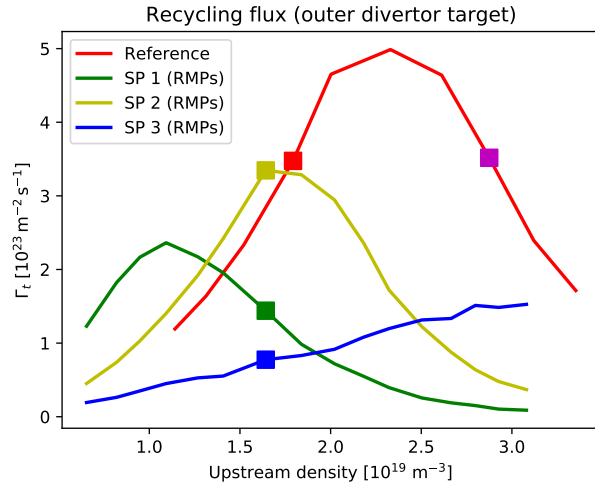
Figure 9. Density scan of the local ion (recycling) flux Γ_t on the outer divertor target evaluated at 3 points of the RMP strike area compared to the reference case without RMPs. Squares mark the simulations shown in figure 5 (d) without RMPs and (f) with RMPs, except for the magenta point which links to profile of the same colour in figure 10 (b) for a partially detached reference state at higher $\overline{n}_{\mathrm{up}}$.
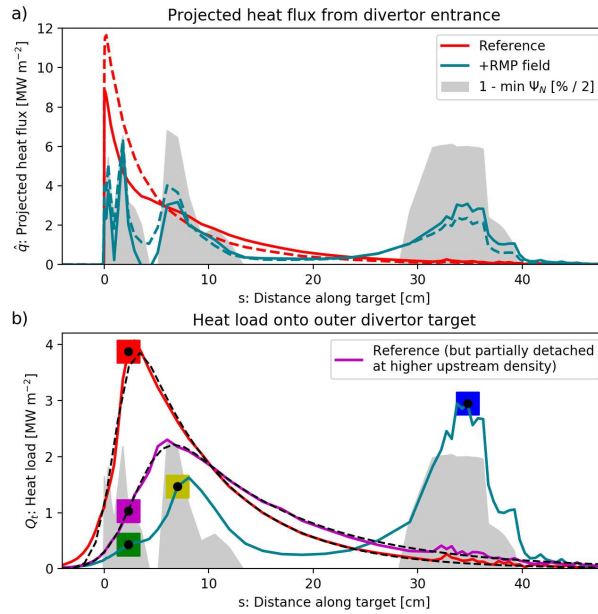

Figure 10. (a) Distribution along the outer divertor target of the projected heat flux $\hat{q}$ from the divertor entrance (solid) and its contributions from heat conduction (dashed) in comparison to where field lines connect from the bulk plasma (gray, taken from figure 5 (c)), and (b) actual heat load Q_t on the outer divertor target with and without RMPs. Coloured points link to figure 9, and black dashed lines are fits to (8).

attached throughout the entire density scan.

Partial detachment traditionally refers to the state where the plasma at the strike zone near the separatrix is detached while the plasma at the strike zone further away

remains attached. Qualitatively, this characterization may apply to the RMP case as well, but one should note that it is quantitatively very different because of the different exhaust mechanisms (SOL field lines with plasma provided by cross-field transport through the separatrix vs. transport along perturbed field lines directly from the bulk plasma). The implications of this difference become clear by evaluating exhaust from the bulk plasma at the divertor entrance. Figure 10 (a) shows the upstream heat flux at the divertor entrance mapped to the target:

$$\hat{q} = q_{u\parallel} \frac{B_t}{B_u} \sin\theta \tag{6}$$

which is the heat flux that would be deposited on the target from a parallel heat flux $q_{u\parallel}$ entering the divertor (evaluated just above the X-point) without any form of dissipation. For the sake of this argument, $q_{u\parallel}$ is mapped onto the target and not to the outboard midplane as is usually done for evaluation of the SOL width in the form of an e-folding length, because our focus is on the relation between $\hat{q}$ and the actual deposited heat flux q_t. Nevertheless, the exponential character of the conductive heat flux can be seen in figure 10 (a) for the unperturbed reference case (red dashed line). The total $\hat{q}$ includes convection, and residual effects of a flow-reversal near the separatrix can be seen here. The plasma heat load (not accounting for contributions from neutral particles and radiation)

$$Q_t = q_t + \varepsilon\,\Gamma_t. \tag{7}$$

on the divertor target is shown by the red line in figure 10 (b), and it should be noted that this includes the released potential energy $\varepsilon \approx 13.6 + 2\,\text{eV}$ from recombination of the incident ion and electron flux into atoms and further recombination into molecules. It can be seen that the peak heat load in the unperturbed reference (red) does not occur at the separatrix strike point, but rather a few cm into the SOL. This is because of diffusion into the private flux region and losses from neutral gas interactions (excitation, molecular dissociation and ionization), as we shall evaluate below. The resulting profile is well captured by a convolution of an exponential with a Gaussian [47]

$$Q_t \approx \frac{Q_0}{2}\,\exp\left[\left(\frac{S}{2\lambda\,f_x}\right)^2 - \frac{s - s_0}{\lambda\,f_x}\right] \cdot \text{erfc}\left(\frac{S}{2\lambda\,f_x} - \frac{s - s_0}{S}\right), \tag{8}$$

as evidenced by the black dashed line on top of the red one in figure 10 (b). Here, characteristic parameters are the peak heat flux projected from the divertor entrance (Q_0), the radial decay length (λ) of a purely exponential parallel heat flux profile, the effective flux expansion on the target (f_x), and the power spreading factor (S) for diffusive heat transport into the private flux region between the X-point and the divertor target. It should be noted that s_0 is included as a fit parameter here, while s is already defined as the distance from the separatrix strike point. This is because (8) accounts for broadening of the heat load profile from diffusion, but not for localized losses e.g. from neutral gas interactions. The latter may have the net effect of removing the initial
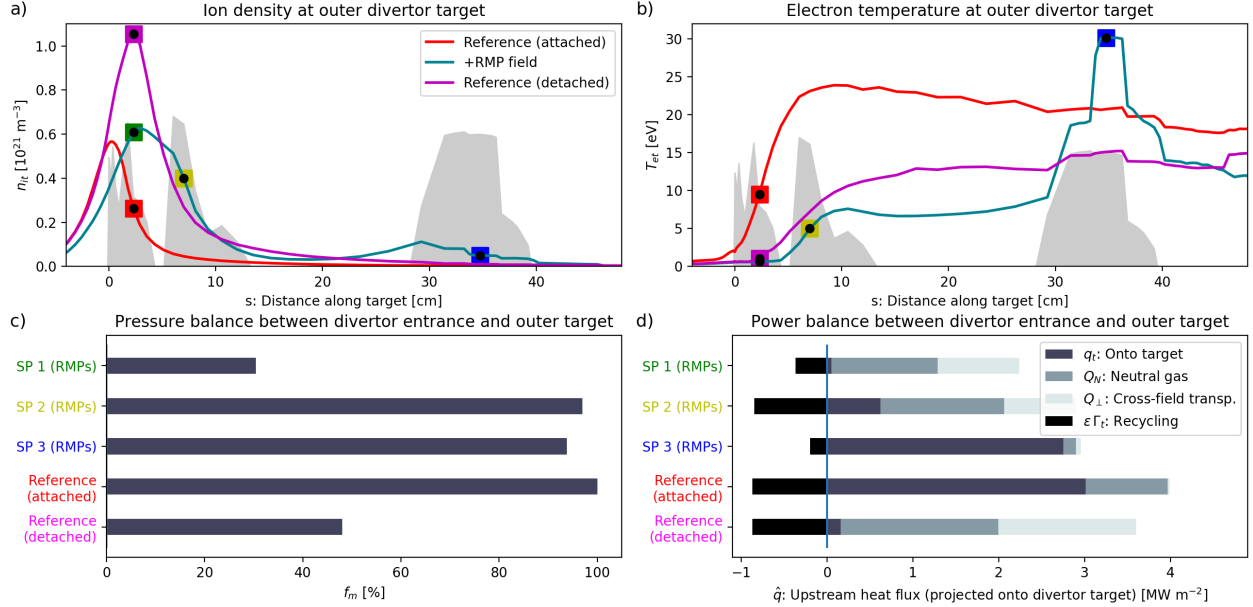
Figure 11. Ion density (a) and temperature (b) at the outer divertor target for the RMP case (green) compared to the reference case (red) at the same upstream density. Profiles for a partially detached reference case at higher upstream density are shown in magenta, and strike points from field lines connecting from the bulk plasma are highlighted in gray. Colored points link to figure 9. (c) Pressure and (d) power balance between divertor entrance and target for the example strike points.

part of the exponential heat flux that went into the convolution, resulting in (8) with an offset s_0. In this regard, s_0 may characterize the extent of partial detachment in the axisymmetric equilibrium configuration. As discussed above, the red reference point marked in figure 10 (b) is still attached, and $s_0 = 1.1 \, \text{cm} < s_1$ (i.e. the example strike point position) supports this observation. A partially detached state at higher density can be identified by the magenta mark in figure 9, and the corresponding Q_t is shown by the magenta profile in figure 10 (b). The shape of this profile is still represented by (8), but now $s_0 = 3.1 > s_1$ consistent with detachment at the reference point s_1. The heat flux width implied by (8) is given by [48] (note that our definition follows reference [47] in that S already includes the flux expansion factor f_x)

$$w \approx \lambda \, f_x + 1.64 \, S \tag{9}$$

which increases from $11.6 \, \text{cm}$ in the attached case to $17.5 \, \text{cm}$ in the partially detached case. Nevertheless, this is still much smaller than the magnetic footprint splitting with RMPs.

We have seen that particle flux roll-over has already occurred at SP 1 (green) in the RMP case at the same $\overline{n}_{\text{up}}$, and that low heat loads are found here. From figure 10 (a) we find that power exhaust is distributed over field lines connecting from the bulk plasma in the RMP case (green): qualitatively the same $\hat{q}$ is connected to the SP 1 in the traditional strike zone and SP 3 in the far SOL, in stark contrast to the exponential-like
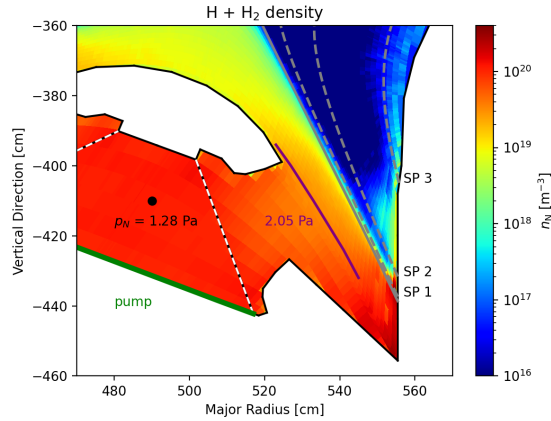
Figure 12. Neutral density $n_N = n_H + n_{H_2}$ at $\varphi = 75$ deg with RMPs for $\overline{n}_{up} = 1.6 \cdot 10^{19}\,m^{-3}$ (i.e. the simulation marked with squares in figure 9) Dashed gray lines are projections of field lines connecting to strike points SP 1 - 3. The purple line highlights the range which is used in SOLPS-ITER simulations for evaluation of the divertor neutral pressure [3] (with a similar range at the inner divertor)

shape of $\hat{q}$ in the reference case. As a result, $\hat{q}$ for SP 1 is significantly lower than in the reference case, which motivates the earlier detachment transition with RMPs. This is supported in figure 11 by much lower $T_{et} = 0.65\,eV$ compared to $T_{et} = 9.5\,eV$, and lower pressure despite a factor 2 higher n_{it}. The ratio $f_m = p_t/p_u$ of total (static + dynamic) pressure at the target and divertor entrance is shown in figure 11 (c), and it can be seen that momentum dissipation has already set in at SP 1 with RMPs - but not in the reference case without RMPs, or at SP 2 with RMPs which is just at the roll-over point. By integrating (3) along a field line, we can link q_t to $\hat{q}$:

$$q_t = \hat{q} - Q_\perp - Q_N, \tag{10}$$

and evaluate Q_N and $Q_\perp$ from simulation results. Here, the integrals Q_N and $Q_\perp$ represent, respectively, the heat flux spent on excitation, molecular dissociation and ionization of neutral gas, and the net heat flux lost (on this field line) from cross-field transport. Figure 11 (d) shows the integrated balance (10), and the additional $\varepsilon\,\Gamma_t$ (that is not provided by $\hat{q}$) is included as an extension on the left hand side. It can be seen that both neutral gas interactions and cross-field transport play a major role for SP 1, which together dissipate almost all of $\hat{q}$. This is similar to the detached state of the reference case at higher $\overline{n}_{up}$ (magenta), while most $\hat{q}$ is still deposited on the target for the same $\overline{n}_{up}$ (red).

Further into the SOL, on the other hand, SP 3 remains attached at this $\overline{n}_{up}$, and no pressure drop between divertor entrance and target is found. Unlike the partially detached state of the reference case, however, significant heat loads are deposited in the far SOL at SP 3 connected to high $\hat{q}$ (whereas $\hat{q}$ is negligible here in the reference case). Figure 11 also shows that a high $T_{et} \approx 30\,eV$ is found at SP 3, with a value of

$n_{it} \approx 5 \cdot 10^{19} \, \mathrm{m}^{-3}$ that is an order of magnitude lower than at SP 1 (but still an order of magnitude higher than in the reference case at the same location). The high T_{et} is related to a shorter field line connection $L_3 = 14.6 \, \mathrm{m}$ from the divertor entrance to the target compared to SP 1 with $L_1 = 35.5 \, \mathrm{m}$ (because field lines pass the X-point at a greater radial distance), which brings a tighter coupling between the bulk plasma upstream and the divertor plasma downstream. But it is not just a matter of how RMPs restructure the upstream plasma, RMP effects on detachment are also determined by the recycling properties of the divertor. The vertical targets in ITER are designed to favour reflection of recycled neutral particles from the SOL towards the private flux region (in order to efficiently pump from below the dome). Therefore, as can be seen in figure 12, density buildup from recycling is more efficient at SP 1 and (to some extent at) SP 2, while SP 3 is starved from recycled neutral particles and remains in a low (linear) recycling state. This is opposite to observations in an open flat divertor configuration at DIII-D with RMPs [49, 50] where the divertor geometry favours the reflection of recycled neutral particles towards the far-SOL plasma [51]. The divertor neutral pressure (which is about a factor 2 higher than the value in the volume below the dome, as shown in figure 12) is found to be in the range of $0.5 - 7 \, \mathrm{Pa}$ for the density scan in figure 9. The opacity of the divertor plasma is high and increases with density: only a fraction of about 10^{-3} of the ionization occurs inside the bulk plasma. The opacity remains high when RMPs are included, but increases somewhat less at higher density)

The present results appear to contradict observations at ASDEX Upgrade [52] where the heat flux striations from RMP application are washed out in the detached state. This requires further evaluation, and in the following we motivate that this qualitative difference is likely attributed to the magnetic footprint size s_ψ relative to the heat flux width w (and in particular the power spreading factor S) of the unperturbed configuration. For ITER, we have found that w is still considerably smaller than s_ψ, even after broadening in the partially detached case. Hence, the heat load striation pattern with RMPs is dominated by parallel transport along perturbed field lines from the bulk plasma. In ASDEX Upgrade, on the other hand, $s_\psi \approx 1 - 2 \, \mathrm{cm}$ appears to be rather small (approximated from the envelope of field lines with long connection length in figure 5.10 in reference [53] and figure 9 in reference [54]). Already the attached configuration (32217) exhibits a qualitative difference: the heat flux width (9) of the unperturbed configuration is given by $\lambda f_x = 1.80 \, \mathrm{cm}$ and $1.64 \, S = 2.56 \, \mathrm{cm}$ [55] (which already includes the flux expansion factor $f_x = 4.88$ for this ASDEX Upgrade discharge). Hence, almost all of the observed heat flux striation in this case is attributed to the ripple in the scrape-off layer beyond s_ψ which is caused by the corrugation of the separatrix, rather than from transport along perturbed field lines directly from the bulk plasma. In the detached case at high density (32922), S increases by a factor of 15 [52] so that the heat load pattern is entirely dominated by cross-field diffusion. Therefore, qualitative differences between ITER and ASDEX Upgrade are to be expected as long as the prediction of s_ψ relative to w holds.
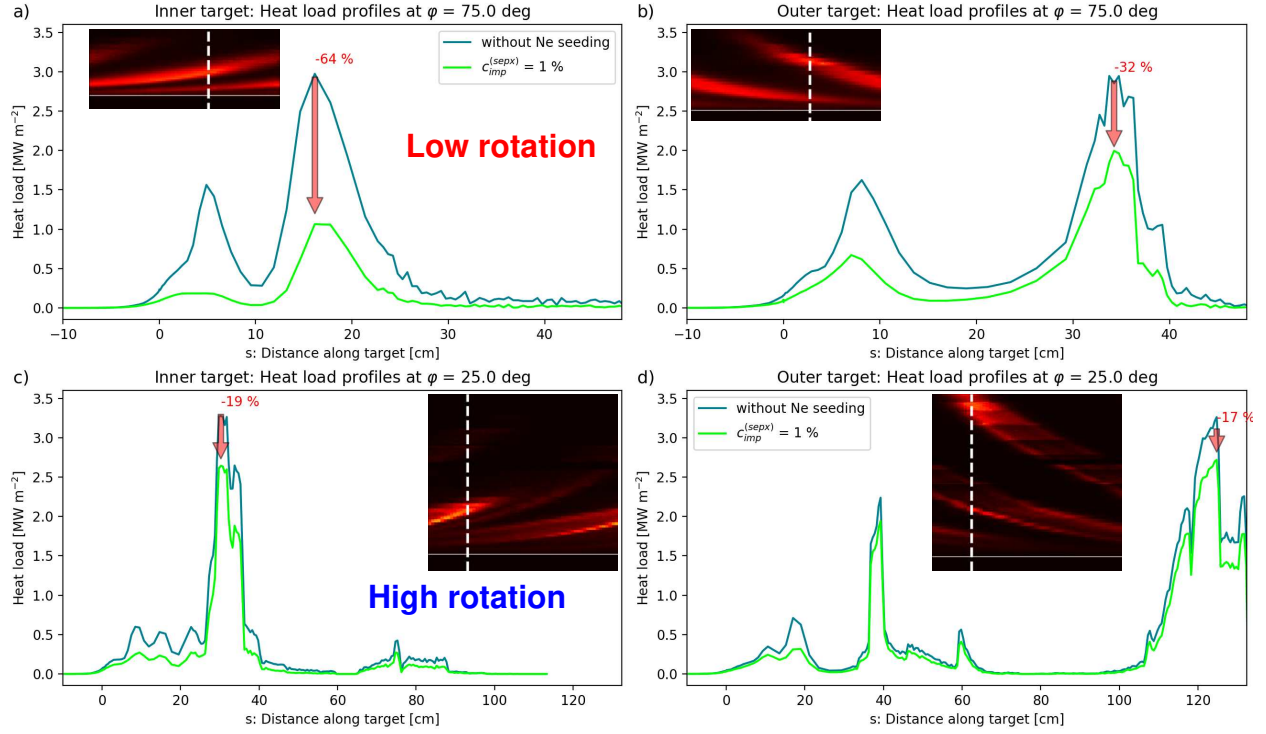
Figure 13. Heat load profiles on the inner (left) and outer (right) divertor targets for the low rotation (upper row) and high rotation plasma response case (lower row) for $\Phi_{\text{gas}} = 3 \cdot 10^{22}\,\text{s}^{-1}$.

3.2. Neon seeding

A second route to detachment (besides increasing the upstream density) is through dissipation from seeded impurities. Presently, neon (Ne) is the favoured species for the burning plasma phase in ITER, but options include nitrogen and argon. In the following simulations, Ne is seeded through a gas puff from the top of the device along with the main species. The source strength is scaled to match an average concentration of $1\,\%$ at $\psi_N = 1$. Pumping of impurities is not implemented at this point, but removal of impurities is approximated by a recycling coefficient of $99\,\%$. As mentioned in section 2, the impact of impurities on the main species in the EMC3-EIRENE *trace* approximation is an additional cooling term $S_{ee,imp}$ in the electron energy balance (3). Dissipation from impurity radiation depends on the electron density and temperature, and its efficiency may therefore be impacted by RMPs.

Heat loads are shown in figure 13 for the inner and outer targets, and for the two different plasma response cases discussed in section 2.2. Our focus here is on the impact on the outermost non-axisymmetric peak, because heat loads to the traditional strike zone are already significantly reduced as discussed above. Toroidal locations for the profiles are chosen such that far-SOL peaks are captured, as can be seen in the insets for guidance. For the low rotation case (in which the magnetic footprint stays on the vertical target), it can be seen in figure 13 (b) that a moderate reduction of $-32\,\%$

can be achieved for the outermost peak on the outer target. This is promising, keeping in mind that the PFPO phase has lower upstream pressure than the burning plasma phase, which may limit divertor density and impurity radiation here. This is supported by figure 13 (a) which shows a stronger reduction of the peak heat load by -64% at the inner target, consistent with higher density ($3 \cdot 10^{20}\,\mathrm{m^{-3}}$ vs. $4 \cdot 10^{19}\,\mathrm{m^{-3}}$) and lower temperature ($4\,\mathrm{eV}$ vs. $25\,\mathrm{eV}$) here compared to the outer target peak. Heat loads peaks in the traditional strike zone are reduced to values below $0.2\,\mathrm{MW\,m^{-2}}$ on the inner target, and $0.7\,\mathrm{MW\,m^{-2}}$ on the outer target at densities of $3.6 - 5 \cdot 10^{20}\,\mathrm{m^{-3}}$.

The beneficial impact of Ne seeding is much less effective for the high rotation plasma case in which the magnetic footprint extends onto the curved divertor baffle. It can be seen in figure 13 (d) that a small reduction (-17%) of the heat load onto the curved baffle is possible, despite the rather small density of $6 \cdot 10^{18}\,\mathrm{m^{-3}}$ there. The high heat load at this location is caused by the high temperature of $75\,\mathrm{eV}$, which can pose an issue regarding the exposed edges of the monoblocks and tungsten sputtering. Even on the inner target, the heat load peak corresponds to a relatively low density of $2.5 \cdot 10^{19}\,\mathrm{m^{-3}}$ and high temperature of $46\,\mathrm{eV}$, and only a moderate reduction (-19%) of the heat load to a level of $2.6\,\mathrm{MW\,m^{-2}}$ is found. Significantly higher peak densities of $3 - 4 \cdot 10^{20}\,\mathrm{m^{-3}}$ at temperature of $\sim 1\,\mathrm{eV}$ are found in the traditional strike zone, but heat loads are small there to begin with. It should be noted, however, that the high rotation case is considered to be less likely than the low rotation case since it requires $10\,\mathrm{MW}$ of NBI injection. Nevertheless, since a similar extension of the magnetic footprint may already be present at moderate plasma rotation (with similar results expected for heat loads), it is essential to verify plasma response models with respect to their impact on the plasma boundary.

4. Discussion and conclusions

Following substantial upgrades of EMC3-EIRENE for modelling of the detached divertor plasma state [31] (numerical stabilization at low divertor temperatures and implementation of volumetric recombination), an assessment of RMP effects on the edge and divertor plasma in ITER has been presented which for the first time goes significantly beyond an earlier exploration of the attached divertor state [28] (which will be completely inaccessible during burning plasma operation from the point of view of divertor target power handling). Here, we have focused on hydrogen H-mode plasmas at $5\,\mathrm{MA}/1.8\,\mathrm{T}$ at the standard $q_{95} \approx 3$ during the first pre-fusion power operation phase, because these plasmas allow for exploration of (how RMPs affect) the transition from an attached to a detached divertor state. Exhaust from the bulk plasma is guided by the helical corrugations of the perturbed separatrix, and this results in a more distributed heat flux at the divertor entrance compared to the traditional exponential-like profile. As a consequence, an earlier onset of detachment (i.e. at lower upstream density) is found in the traditional strike zone when RMPs are applied, but secondary, non-axisymmetric strike locations appear - and remain attached with target plasma temperatures above

10 eV. It is important to note that even higher upstream temperatures are expected for the burning plasma phase at full power, and this may lead to even more problematic conditions downstream (power fluxes and tungsten sputtering) at the far-SOL strike locations. Further developments of EMC3-EIRENE (e.g. $\mathbf{E} \times \mathbf{B}$ drifts, and heat flux and viscosity limits) are required in order to catch up with contemporary 2-D models, and this may improve the reliability of predictions for RMP effects on the plasma boundary. For example, the upstream heat flux in the perturbed bulk plasma can be of similar value as the free streaming limit due to the low collisionality, and this may underestimate the broadening of the upstream profiles from cross-field diffusion.

An initial assessment of Neon seeding has shown that the non-axisymmetric far-SOL heat loads can be mitigated. However, impurity radiation does not appear to be as effective at the far-SOL strike locations compared to the traditional strike zone, which is consistent with lower density in the far-SOL. In particular, dissipation from impurity seeding is found to be more effective for the inner target (where the magnetic footprint tends to be more compact) than for the outer target, and becomes ineffective when the magnetic footprint extends beyond the straight, optimized region onto the curved baffle region. Further investigation for higher upstream density or impurity concentration is suggested.

The present simulations include plasma response effects from a linearized, resistive, single fluid MHD model, and it has been shown that a significant temperature drop in the edge from application of the vacuum approximation of the RMP field can be avoided once screening of the RMP field is taken into account. However, it is also shown that the MARS-F plasma response includes field amplification near the separatrix, and this is found to play a pivotal role for the magnetic footprint on the divertor targets. A significant extension of the footprint beyond the optimized high heat flux regions of the ITER vertical targets is found to be possible, but is sensitive to model parameters related to the level of toroidal rotation in the plasma. Therefore, further evaluation and verification of the plasma response is key for reliable predictions of divertor heat and particles fluxes. A variety of MHD models exist besides MARS-F that predict the plasma response (IPEC [56, 57], GPEC [58], HINT [59], JOREK [54], M3D-C1 [60, 61]). A review of MHD models is given in reference [41], but it is found that different models come to different results when applied to a selected configuration [62]. Presently, no plasma response model exists that reproduces both upstream and downstream observations [63]. Further evaluation of the sensitivity of the plasma boundary to plasma response model parameters (and verification for present experiments) is advisable. Ultimately, however, a self-consistent integration of the plasma response and the boundary plasma may become necessary to provide a full physics model to provide accurate predictions for ITER.

Acknowledgments

References

[1] ITER Organization. ITER Research Plan within the Staged Approach. Technical Report ITR-18-003, ITER Organization, 2018.

[2] R.A. Pitts, S. Bardin, B. Bazylev, M.A. van den Berg, P. Bunting, S. Carpentier-Chouchana, J.W. Coenen, Y. Corre, R. Dejarnac, F. Escourbiac, J. Gaspar, J.P. Gunn, T. Hirai, S-H. Hong, J. Horacek, D. Iglesias, M. Komm, K. Krieger, C. Lasnier, G.F. Matthews, T.W. Morgan, S. Panayotis, S. Pestchanyi, A. Podolnik, R.E. Nygren, D.L. Rudakov, G. De Temmerman, P. Vondracek, and J.G. Watkins. Physics conclusions in support of ITER W divertor monoblock shaping. *Nuclear Materials and Energy*, 12:60, 2017.

[3] R.A. Pitts, X. Bonnin, F. Escourbiac, H. Frerichs, J.P. Gunn, T. Hirai, A.S. Kukushkin, E. Kaveeva, M.A. Miller, D. Moulton, V. Rozhansky, I. Senichenkov, E. Sytova, O. Schmitz, P.C. Stangeby, G. De Temmerman, I. Veselova, and S. Wiesen. Physics basis for the first ITER tungsten divertor. *Nuclear Materials and Energy*, 20:100696, 2019.

[4] G. F. Matthews. Plasma detachment from divertor targets and limiters. *J. Nucl. Mater.*, 220-222:104–116, 1995.

[5] S. I. Krasheninnikov and A. S. Kukushkin. Physics of ultimate detachment of a tokamak divertor plasma. *J. Plasma Phys.*, 83(5):155830501, 2017.

[6] P. C. Stangeby. Basic physical processes and reduced models for plasma detachment. *Plasma Phys. Control. Fusion*, 60:044022, 2018.

[7] A.S. Kukushkin, H.D. Pacher, V. Kotov, G.W. Pacher, and D. Reiter. Finalizing the ITER divertor design: The key role of SOLPS modeling. *Fusion Eng. Des.*, 86:2865, 2011.

[8] H.D. Pacher, A.S. Kukushkin, G.W. Pacher, V. Kotov, R.A. Pitts, and D. Reiter. Impurity seeding in ITER DT plasmas in a carbon-free environment. *J. Nucl. Mater.*, 463:591, 2015.

[9] H. Zohm. Edge localized modes (ELMs). *Plasma Phys. Control. Fusion*, 38:105–128, 1996.

[10] T. E. Evans, R. A. Moyer, P. R. Thomas, J. G. Watkins, T. H. Osborne, J. A. Boedo, E. J. Doyle, M. E. Fenstermacher, K. H. Finken, R. J. Groebner, M. Groth, J. H. Harris, R. J. La Haye, C. J. Lasnier, S. Masuzaki, N. Ohyabu, D. G. Pretty, T. L. Rhodes, H. Reimerdes, D. L. Rudakov, M. J. Schaffer, G. Wang, and L. Zeng. Suppression of Large Edge-Localized Modes in High-Confinement DIII-D Plasmas with a Stochastic Magnetic Boundary. *Phys. Rev. Lett.*, 92(23):235003, 2004.

[11] Y. Liang, H. R. Koslowski, P. R. Thomas, E. Nardon, B. Alper, P. Andrew, Y. Andrew, G. Arnoux, Y. Baranov, M. Becoulet, M. Beurskens, T. Biewer, M. Bigi, K. Crombe, E. De La Luna, P. de Vries, W. Fundamenski, S. Gerasimov, C. Giroud, M. P. Gryaznevich, N. Hawkes, S. Hotchin, D. Howell, S. Jachmich, V. Kiptily, L. Moreira, V. Parail, S. D. Pinches, E. Rachlew, and O. Zimmermann. Active Control of Type-I Edge-Localized Modes with n=1 Perturbation Fields in the JET Tokamak. *Phys. Rev. Lett.*, 98(265004):1–5, 2007.

[12] W. Suttrop, T. Eich, J. C. Fuchs, S. Günter, A. Janzer, A. Herrmann, A. Kallenbach, P. T. Lang, T. Lunt, M. Maraschek, R. M. McDermott, A. Mlynek, T. Pütterich, M. Rott, T. Vierle, E. Wolfrum, Q. Yu, I. Zammuto, H. Zohm, and ASDEX Upgrade Team. First Observation of Edge Localized Modes Mitigation with Resonant and Nonresonant Magnetic Perturbations in ASDEX Upgrade. *Phys. Rev. Lett.*, 106:225004, 2011.

[13] Y. M. Jeon, J.-K. Park, S. W. Yoon, W. H. Ko, S. G. Lee, K. D. Lee, G. S. Yun, Y. U. Nam, W. C.

Kim, Jong-Gu Kwak, K. S. Lee, H. K. Kim, and H. L. Yang. Suppression of Edge Localized Modes in High-Confinement KSTAR Plasmas by Nonaxisymmetric Magnetic Perturbations. *Phys. Rev. Lett.*, 109:035004, 2012.

[14] A. Loarte, G. Huijsmans, S. Futatani, L.R. Baylor, T.E. Evans, D. M. Orlov, O. Schmitz, M. Becoulet, P. Cahyna, Y. Gribov, A. Kavin, A. Sashala Naik, D.J. Campbell, T. Casper, E. Daly, H. Frerichs, A. Kischner, R. Laengner, S. Lisgo, R.A. Pitts, G. Saibene, and A. Wingen. Progress on the application of ELM control schemes to ITER scenarios from the non-active phase to DT operation. *Nuclear Fusion*, 54:033007, 2014.

[15] J. Guckenheimer and P. Holmes. *Nonlinear Oscillations, Dynamical Systems, and Bifurcations of Vector Fields*, volume 42. Applied Mathematical Science, 1983.

[16] A. J. Lichtenberg and M. A. Lieberman. *Regular and chaotic dynamics*. Applied mathematical sciences 38, 2nd edition, 1992.

[17] T. E. Evans, R. K. W. Roeder, J. A. Carter, and B. I. Rapoport. Homoclinic tangles, bifurcations and edge stochasticity in diverted tokamaks. *Contrib. Plasma Phys.*, 44:235–240, 2004.

[18] T. Lunt, Y. Feng, M. Bernet, A. Herrmann, P.de Marne, R. McDermott, H.W. Müller, S. Potzel, T. Pütterich, S. Rathgeber, W. Suttrop, E. Viezzer, E. Wolfrum, M. Willensdorfer, and the ASDEX Upgrade team. First EMC3-Eirene simulations of the edge magnetic perturbations at ASDEX Upgrade compared with the experimen. *Nuclear Fusion*, 52:054013, 2012.

[19] T. E. Evans, R. K. W. Roeder, J. A. Carter, B. I. Rapoport, M. E. Fenstermacher, and C. J. Lasnier. Experimental signatures of homoclinic tangles in poloidally diverted tokamaks. *J. Phys. Conf. Ser.*, 7:174, 2005.

[20] O. Schmitz, T.E. Evans, M.E. Fenstermacher, H. Frerichs, M.W. Jakubowski, M.J. Schaffer, A. Wingen, W.P. West, N.H. Brooks, K.H. Burrell, J.S. deGrassie, Y. Feng, K.H. Finken, P. Gohil, M. Groth, I. Joseph, C.J. Lasnier, M. Lehnen, A.W. Leonard, S. Mordijck, R.A. Moyer, A. Nicolai, T.H. Osborne, D. Reiter, U. Samm, K.H. Spatschek, H. Stoschus, B. Unterberg, E.A. Unterberg, J.G. Watkins, R. Wolf, and the DIII-D and TEXTOR Teams. Aspects of three dimensional transport for ELM control experiments in ITER-similar shape plasmas at low collisionality in DIII-D. *Plasma Phys. Control. Fusion*, 50:124029, 2008.

[21] M. Jia, Y. Sun, F. Zhong, H. Li, G. Li, L. Wang, K. Gan, B. Zhang, J. Qian, and B. Shen. Vacuum modeling of three-dimensional magnetic field topology under resonant magnetic perturbations on EAST. *Plasma Phys. Control. Fusion*, 58:055010, 2016.

[22] D.M. Harting, Y. Liang, S. Jachmich, R. Koslowski, G. Arnoux, S. Devaux, T. Eich, E. Nardon, D. Reiter, H. Thomsen, and JET EFDA contributors. Strike point splitting in the heat and particle flux profiles compared with the edge magnetic topology in a n = 2 resonant magnetic perturbation field at JET. *Nuclear Fusion*, 52:054009, 2012.

[23] K. Kim, J.-W. Ahn, H. H. Lee, J.-K. Park, C. S. Kang, Y. In, J. G. Kwak, S. W. Yoon, O. K. Oh, and W. Choe. Comparison of divertor heat flux splitting by 3D fields with field line tracing simulation in KSTAR. *Phys. Plasmas*, 24:052506, 2017.

[24] J.-W. Ahn, J.M. Canik, V.A. Soukhanovskii, R. Maingi, and D.J. Battaglia. Modification of divertor heat and particle flux profiles with applied 3D fields in NSTX H-mode plasmas. *Nuclear Fusion*, 50:045010, 2010.

[25] Y. Feng, F. Sardei, J. Kisslinger, P. Grigull, K. McCormick, and D. Reiter. 3D Edge Modeling and Island Divertor Physics. *Contrib. Plasma Phys.*, 44(1-3):57–69, 2004.

[26] Y. Feng, H. Frerichs, M. Kobayashi, A. Bader, F. Effenberg, D. Harting, H. Hoelbe, J. Huang, G. Kawamura, J. D. Lore, T. Lunt, D. Reiter, O. Schmitz, and D. Sharma. Recent Improvements in the EMC3-Eirene Code. *Contrib. Plasma Phys.*, 54(4-6):426–431, 2014.

[27] H. Frerichs, D. Reiter, Y. Feng, and D. Harting. Block-structured grids in Lagrangian 3D edge plasma transport simulations. *Comp. Phys. Commun.*, 181:61–70, 2010.

[28] O. Schmitz, M. Becoulet, P. Cahyna, T.E. Evans, Y. Feng, H. Frerichs, A. Loarte, R.A. Pitts, D. Reiser, M.E. Fenstermacher, D. Harting, A. Kirschner, A. Kukushkin, T. Lunt, G. Saibene, D. Reiter, U. Samm, and S. Wiesen. Three-dimensional modeling of plasma edge transport and

divertor fluxes during application of resonant magnetic perturbations on ITER. *Nuclear Fusion*, 56(6):066008, 2016.

[29] H. Frerichs and D. Reiter. Stability and control of iterated non-linear transport solvers for fusion edge plasmas. *Comp. Phys. Commun.*, 188:82, 2015.

[30] H. Frerichs, X. Bonnin, Y. Feng, A. Loarte, R.A. Pitts, D. Reiter, and O. Schmitz. Stabilization of EMC3-EIRENE for detachment conditions and comparison to SOLPS-ITER. *Nuclear Materials and Energy*, 18:62–66, 2019.

[31] H. Frerichs, Y. Feng, X. Bonnin, R. A. Pitts, D. Reiter, and O. Schmitz. Volumetric recombination in EMC3-EIRENE: implementation, and first application to the pre-fusion power operation phase in ITER. *Phys. Plasmas*, (to be submitted to), 2021.

[32] T. Lunt, H. Frerichs, M. Bernert, D. Brida, D. Carralero, M. Cavedon, P. David, A. Drenik, M. Faitsch, Y. Feng, M. Griener, A. Herrmann, B. Kurzan, O. Pan, U. Plank, D. Silvagni, M. Willensdorfer, M. Wischmeier, E. Wolfrum, and the ASDEX Upgrade team. Near- and far scrape-off layer transport studies in detached, small-ELM ASDEX Upgrade upper single-null discharges by means of EMC3-EIRENE. *Plasma Phys. Control. Fusion*, 62:105016, 2020.

[33] J. P. Gunn, S. Carpentier-Chouchana nad F. Escourbiac, T. Hirai, S. Panayotis, R.A. Pitts, Y. Corre, R. Dejarnac, M. Firdaouss, M. Kočan, M. Komm, A. Kukushkin, P. Languille, M. Missirlian, W. Zhao, and G. Zhong. Surface heat loads on the ITER divertor verticaltargets. *Nuclear Fusion*, 57:046025, 2017.

[34] M. Schneider, A.R. Polevoi, S.H. Kim, A. Loarte, S.D. Pinches, J-F. Artaud, E. Militello-ASP, B. Beaumont, R. Bilato, D. Boilson, D.J. Campbell, P. Dumortier, D. Farina, L. Figini, Y. Gribov, M. Henderson, R.R. Khayrutdinov, A.A. Kavin, F. Köchl, T. Kurki-Suonio, A. Kuyanov, P. Lamalle, E. Lerche, V.E. Lukash, A. Messiaen, V. Parail, K. Särkimäki, A. Snicker, D. Van Eester, and the ITPA Topical Groups on Energetic Particle Physics and Integrated Operation & Scenarios. Modelling one-third field operation in the ITER pre-fusion power operation phase. *Nuclear Fusion*, 59:126014, 2019.

[35] A. Loarte. *Nuclear Fusion*, (to be published), 2021.

[36] L. Li, Y. Q. Liu, N. Wang, A. Kirk, H. R. Koslowski, Y. Liang, A. Loarte, D. Ryan, and F. C. Zhong. Toroidal modeling of plasma response to RMP fields in ITER. *Plasma Phys. Control. Fusion*, 59:044005, 2017.

[37] L. Li, Y. Q. Liu, A. Loarte, S. D. Pinches, A. Polevoi, Y. Liang, and F. C. Zhong. Modeling 3D plasma boundary corrugation and tailoring toroidal torque profiles with resonant magnetic perturbation fields in ITER. *Nuclear Fusion*, 59:096038, 2019.

[38] Y. Q. Liu, A. Bondeson, C. M. Fransson, B. Lennartson, and C. Breitholtz. Feedback stabilization of nonaxisymmetric resistive wall modes in tokamaks. I. Electromagnetic model. *Phys. Plasmas*, 7:3681, 2000.

[39] Y Liu, A. Kirk, and E. Nardon. Full toroidal plasma response to externally applied nonaxisymmetric magnetic fields. *Phys. Plasmas*, 17:122502, 2010.

[40] Y. Feng, F. Sardei, and J. Kisslinger. A simple highly accurate field-line mapping technique for three-dimensional Monte Carlo modeling of plasma edge transport. *Phys. Plasmas*, 12(052505):1–7, 2005.

[41] Y. Liu, C. J. Ham, A. Kirk, L. Li, A. Loarte, D. A. Ryan, Y. Sun, W. Suttrop, X. Yang, and L. Zhou. ELM control with RMP: plasma response models and the role of edge peeling response. *Plasma Phys. Control. Fusion*, 58:114005, 2016.

[42] S. R. Hudson and J. Breslau. Temperature Contours and Ghost Surfaces for Chaotic Magnetic Fields. *Phys. Rev. Lett.*, 100:095001, 2008.

[43] H. Frerichs, D. Reiter, O. Schmitz, P. Cahyna, T. Evans, Y. Feng, and E. Nardon. Impact of screening of resonant magnetic perturbations in 3D edge plasma transport simulations for DIII-D. *Phys. Plasmas*, 19:052507, 2012.

[44] X. Yang, Y. Liu, C. Paz-Soldan, L. Zhou, L. Li, G. Xia, Y. He, and S. Wang. Resistive versus ideal plasma response to RMP fields in DIII-D: roles of q95 and X-point geometry. *Nuclear*

Fusion, 59:086012, 2019.

[45] C. Chrystal, B.A. Grierson, G.M. Staebler, C.C. Petty, W.M. Solomon, J.S. deGrassie, K.H. Burrell, T. Tala, and A. Salmi. Predicting rotation for ITER via studies of intrinsic torque and momentumtransport in DIII-D. *Phys. Plasmas*, 24:056113, 2017.

[46] T. Hirai, S. Carpentier-Chouchana, F. Escourbiac, S. Panayotis, A. Durocher, L. Ferrand, M. Garcia-Martinez, J.P. Gunn, V. Komarov, M. Merola, and R.A. Pitts adn G. De Temmerman. Design optimization of the ITER tungsten divertor vertical targets. *Fusion Engineering and Design*, 127:66–72, 2018.

[47] T. Eich, B. Sieglin, A. Scarabosio, W. Fundamenski, R.J. Goldston, A. Herrmann, and ASDEX Upgrade Team. Inter-ELM Power Decay Length for JETand ASDEX Upgrade: Measurement and Comparison with Heuristic Drift-Based Model. *Phys. Rev. Lett.*, 107:215001, 2011.

[48] M. A. Makowski, D. Elder, T. K. Gray, B. LaBombard, C. J. Lasnier, A. W. Leonard, R. Maingi, T. H. Osborne, P. C. Stangeby, J. L. Terry, and J. Watkins. Analysis of a multi-machine database on divertor heat fluxes. *Phys. Plasmas*, 19:056122, 2012.

[49] H. Frerichs, O. Schmitz, D. Reiter, T. E. Evans, and Y. Feng. Striation pattern of target particle and heat fluxes in three dimensional simulations for DIII-D. *Phys. Plasmas*, 21:020702, 2014.

[50] A.R. Briesemeister, J.-W. Ahn, J.M. Canik, M.E. Fenstermacher, H. Frerichs, C. J. Lasnier, J.D. Lore, A.W. Leonard, M.A. Makowski, A.G. McLean, W.H. Meyer, O. Schmitz, M.W. Shafer, E.A. Unterberg, H.Q. Wang, and J. G. Watkins. Changes in divertor conditions in response to changing core density with RMPs. *Nuclear Fusion*, 57:076038, 2017.

[51] A. Loarte. Effects of divertor geometry on tokamak plasmas. *Plasma Phys. Control. Fusion*, 43:R183, 2001.

[52] D. Brida, T. Lunt, M. Wischmeier, M. Bernert, D. Carralero, M. Faitsch, Y. Feng, T. Sehmer, B. Sieglin, W. Suttrop, E. Wolfrum, The ASDEX Upgrade Team, and The MST1 Team. Heat flux pattern in detached L-modes and ELM mitigated H-modes with rotating magnetic perturbations in ASDEX Upgrade. *Nuclear Fusion*, 57:116006, 2017.

[53] D. Brida. *Experimental and Numerical Investigation of Power Exhaust in the Tokamak ASDEX Upgrade with Magnetic Perturbations*. Dissertation, Technische Universität München, München, 2018.

[54] F. Orain, M. Hölzl, E. Viezzer, M. Dunne, M. Bécoulet, P. Cahyna, G.T.A. Huijsmans, J. Morales, M. Willensdorfer, W. Suttrop, A. Kirk, S. Pamela, S. Günter, K. Lackner, E. Strumberger, A. Lessig, and the ASDEX Upgrade Team and the EUROfusion MST Team. Non-linear modeling of the plasma response to RMPs in ASDEX Upgrade. *Nuclear Fusion*, 57:022013, 2017.

[55] M. Faitsch, B. Sieglin, T. Eich, A. Herrmann, W. Suttrop, and the ASDEX Upgrade Team. Divertor heat load in ASDEX Upgrade L-mode in presence of external magnetic perturbation. *Plasma Phys. Control. Fusion*, 59:095006, 2017.

[56] J.-K. Park, A. H. Boozer, and A. H. Glasser. Computation of three-dimensional tokamak and spherical torus equilibria. *Phys. Plasmas*, 14:052110, 2007.

[57] J.-K. Park, J. E. Menard, A. H. Boozer, M. J. Schaffer, and S. A. Wolfe. Ideal Perturbed Equilibria in Tokamaks and Control of External Magnetic Perturbations. *Contrib. Plasma Phys.*, 50(6-7):669, 2010.

[58] J.-K. Park and N. C. Logan. Self-consistent perturbed equilibrium with neoclassical toroidal torque in tokamaks. *Phys. Plasmas*, 24:032505, 2017.

[59] Yasuhiro Suzuki, Noriyoshi Nakajima, Kiyomasa Watanabe, Yuji Nakamura, and Takaya Hayashi. Development and application of HINT2 to helical system plasmas. *Nuclear Fusion*, 46:L19, 2006.

[60] S. C. Jardin, N. Ferraro, X. Luo, J. Chen, J. Breslau, K. E. Jansen, and M. S. Shephard. The M3D-C^1 approach to simulating 3D 2-fluid magnetohydrodynamics in magnetic fusion experiments . *Journal of Physics: Conference Series*, 125:012044, 2008.

[61] N. M. Ferraro. Calculations of two-fluid linear response to non-axisymmetric fields in tokamaks. *Phys. Plasmas*, 19:056105, 2012.

[62] A. Reiman, N.M. Ferraro, A. Turnbull, J.K. Park, A. Cerfon, T.E. Evans, M.J. Lanctot, E.A. Lazarus, Y.Liu, G. McFadden, D. Monticello, and Y. Suzuki. Tokamak plasma high field side response to an n = 3 magnetic perturbation: a comparison of 3D equilibrium solutions from seven different codes. *Nuclear Fusion*, 55:063026, 2015.

[63] J. D. Lore, A. Briesemeister, N. M. Ferraro, H. Frerichs, B. Lyons, A. McLean, J.-K. Park, and M. Shafer. Pedestal-to-Wall 3D Fluid Transport Simulations on DIII-D. *Nuclear Fusion*, 57:056025, 2017.